

Interplay between Vacuum-Grown Monolayers of Alkylphosphonic Acids and the Performance of Organic Transistors Based on Dinaphtho[2,3-*b*:2',3'-*f*]thieno[3,2-*b*]thiophene

Stuart Hannah,[†] Javier Cardona,[‡] Dimitrios A. Lamprou,[§] Pavol Šutta,^{||} Peter Baran,[⊥] Afra Al Ruzaiqi,[†] Karen Johnston,^{*,‡} and Helena Gleskova^{*,†}

[†]Department of Electronic and Electrical Engineering, University of Strathclyde, 204 George Street, Glasgow G1 1XW, United Kingdom

[‡]Department of Chemical and Process Engineering, University of Strathclyde, James Weir Building, 75 Montrose Street, Glasgow G1 1XJ, United Kingdom

[§]Strathclyde Institute of Pharmacy and Biomedical Sciences, University of Strathclyde, 161 Cathedral Street, Glasgow G4 0RE, United Kingdom

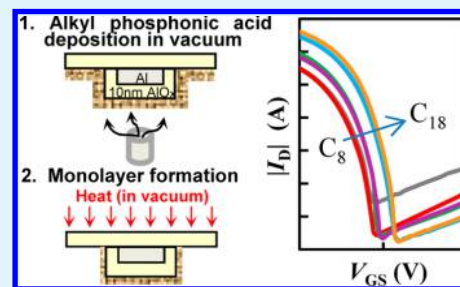
^{||}New Technologies Research Centre, University of West Bohemia, Univerzitní 8, 306 14 Pilsen, Czech Republic

[⊥]Department of Chemistry, Juniata College, 2035 von Liebig Science Center, Huntingdon, Pennsylvania 16652, United States

Supporting Information

ABSTRACT: Monolayers of six alkylphosphonic acids ranging from C₈ to C₁₈ were prepared by vacuum evaporation and incorporated into low-voltage organic field-effect transistors based on dinaphtho[2,3-*b*:2',3'-*f*]thieno[3,2-*b*]thiophene (DNTT). Similar to solution-assembled monolayers, the molecular order for vacuum-deposited monolayers improved with increasing length of the aliphatic tail. At the same time, Fourier transform infrared (FTIR) measurements suggested lower molecular coverage for longer phosphonic acids. The comparison of FTIR and vibration frequencies calculated by density functional theory indicated that monodentate bonding does not occur for any phosphonic acid. All monolayers exhibited low surface energy of ~ 17.5 mJ/m² with a dominating Lifshitz–van der Waals component. Their surface roughness was comparable, while the nanomechanical properties were varied but not correlated to the length of the molecule. However, large improvement in transistor performance was observed with increasing length of the aliphatic tail. Upon going from C₈ to C₁₈, the mean threshold voltage decreased from -1.37 to -1.24 V, the field-effect mobility increased from 0.03 to 0.33 cm²/(V·s), the off-current decreased from $\sim 8 \times 10^{-13}$ to $\sim 3 \times 10^{-13}$ A, and for transistors with $L = 30$ μ m the on-current increased from $\sim 3 \times 10^{-8}$ to $\sim 2 \times 10^{-6}$ A, and the on/off-current ratio increased from $\sim 3 \times 10^4$ to $\sim 4 \times 10^6$. Similarly, transistors with longer phosphonic acids exhibited much better air and bias-stress stability. The achieved transistor performance opens up a completely “dry” fabrication route for ultrathin dielectrics and low-voltage organic transistors.

KEYWORDS: organic field-effect transistors, alkylphosphonic acids, monolayers, DNTT, bias stress



1. INTRODUCTION

The focused improvement of organic field-effect transistors (OFETs) has allowed a whole host of novel demonstrations including radio frequency identification tags,^{1,2} analog and digital circuits,^{3–5} active matrix displays,⁶ and various sensor systems.^{7–9} However, when the application of OFETs in forthcoming areas such as wearable or disposable electronics is considered, low power consumption and low-voltage operation are necessary features, especially for applications powered by batteries or energy-harvesting devices.

A common approach to achieving low-voltage transistor operation is to increase the gate dielectric capacitance by choosing thin layers and/or materials with high relative permittivity (high-*k*). To date, approaches have included single layers of inorganic or organic high-*k* materials, inorganic/

organic bilayers, and organic/inorganic composites.^{10,11} Reduction in the gate dielectric thickness to 10 nm or less typically involves a bilayer, where a medium-*k* to high-*k* inorganic layer is covered with an organic monolayer whose function is to suppress the leakage current, inhibit the surface —OH groups, and reduce the energy of the dielectric surface.^{12–17} In such a case, the transistor operating voltage can be as low as 1.5 V, while the transistor is in the off state at 0 V.^{18–20}

As the thickness of the dielectric is reduced, small variations in its thickness lead to more pronounced variations in its capacitance. Consequently, procedures that inherently lend

Received: July 12, 2016

Accepted: September 1, 2016

Published: September 1, 2016

themselves to good layer uniformity (atomic layer deposition) or self-limit the layer thickness (oxidation or use of monolayers) are advantageous. Aluminum oxide (AlO_x) functionalized with alkylphosphonic acids (C_nPA) is an established bilayer dielectric for low-voltage organic transistors.¹² Such transistors have a bottom-gate structure where the aluminum oxide is commonly prepared by oxidation of the aluminum gate electrode and the assembly of the organic monolayer is performed in solvent-based solutions. A dry route to monolayer assembly has also been demonstrated for *n*-octylphosphonic acids (C₈PA).^{21–23} In such a case, several monolayers of C₈PA were thermally evaporated in vacuum, followed by thermal desorption of all molecules that were not chemically bonded to AlO_x. In such a technique, nonuniformity in the as-deposited C₈PA thickness is eliminated during the second step of thermal desorption, leaving monolayer formation across the substrate. Thermal desorption provides an additional benefit of annealing that improves both the monolayer structure and transistor performance.²³

In this paper we report bottom-gate OFETs based on various AlO_x/C_nPA dielectrics and an air-stable^{24,25} organic semiconductor, dinaphtho[2,3-*b*:2',3'-*f*]thieno[3,2-*b*]thiophene (DNNTT). This was prompted by previous research on solution-assembled C_nPA that observed better transistor performance if longer-chain C_nPA were used. Contrary to solution assembly, this work uses a series of alkylphosphonic acids that were thermally evaporated in vacuum and incorporated into transistors. The dielectrics and the corresponding transistors were fully characterized, including the transistor bias-stress stability. The experiment was accompanied by density functional theory (DFT) calculations to provide insight into the structure of C_nPA monolayers and the corresponding transistor behavior. The achieved transistor performance opens up a completely “dry” fabrication route for ultrathin dielectrics.

2. EXPERIMENTAL SECTION

All samples/devices were fabricated on precleaned Eagle 2000 glass (Scientific Glass). 99.999% aluminum and 99.99% gold were used. Six alkylphosphonic acids with varying length of the aliphatic tail (C₈PA, C₁₀PA, C₁₂PA, C₁₄PA, C₁₆PA, C₁₈PA) were purchased with 97% purity (Strem Chemicals) and purified by recrystallization from hot hexane or heptane solutions with decolorizing charcoal. Dinaphtho[2,3-*b*:2',3'-*f*]thieno[3,2-*b*]thiophene (DNNTT) purified by sublimation was purchased from Sigma–Aldrich.

AlO_x and AlO_x/C_nPA samples for structural and surface characterization were prepared as follows. A 30 nm thick aluminum layer was evaporated on Eagle 2000 glass at a rate of ~2.5 Å/s. Next, approximately 10 nm thick AlO_x was prepared by exposing the aluminum to UV/ozone cleaning system (UVOCS) in ambient atmosphere.²¹ To prevent contamination of the oxidizing surface, the UV/ozone cleaner was enclosed under a high-efficiency particulate air (HEPA) filter. All C_nPA layers were grown in high vacuum in a Mini-Spectros (K. J. Lesker) evaporation chamber enclosed in a N₂-filled glovebox (Jacomex). On the basis of previously optimized C₈PA growth,^{21–23} the evaporation rate of each C_nPA was adjusted to achieve a “monolayer thickness” in about 5.5 s, while the as-deposited thickness was equal to ~9 monolayers. The substrate was kept at room temperature during the evaporation of each C_nPA. Afterward, the substrate temperature was raised to ~160 °C for 3 h to remove all physisorbed molecules. Fourier transform infrared (FTIR) spectroscopy, atomic force microscopy (AFM), and contact angle goniometry (CAG) measurements were performed on such surfaces. In addition, measurements of the AlO_x reference surface (as prepared and annealed for 3 h at ~160 °C) were performed for comparison.

FTIR spectra were measured in reflection mode on a Nicolet 380 spectrometer (Thermo Scientific) equipped with attenuated total reflectance (ATR) accessory with Ge crystal. The beam diameter was ~1.5 mm. The spectral line profile analysis was evaluated by PeakFit software, analyzing the peak positions, full widths at half-maximum (fwhm), integrated intensities (areas below the line profile), and peak heights.

AFM images were obtained by scanning 1 × 1 μm² areas of surface in ambient air by use of a MultiMode 8 scanning probe microscope (Digital Instruments; Bruker Nanoscope analysis software version 1.40) under the new PeakForce quantitative nanomechanical mapping (QNM) mode. The AFM measurements were obtained by use of ScanAsyst air probes. The spring constant (0.47 N/m; nominal 0.4 N/m) and deflection sensitivity have been calibrated, while the nominal value for the tip radius (2 nm) was used. Surface roughness values were determined after employing a digital leveling algorithm (Bruker Image Analysis Nanoscope analysis software v1.5). AFM images were collected at random spots in at least two areas. PeakForce QNM also enables direct extraction of the nanomechanical properties of the samples without damaging them. Each time the tip contacts the sample, the captured force curve is used to calculate the DMT modulus, deformation, energy dissipation, and force of adhesion. To obtain the Young's modulus, the retract curve is fitted by use of the Derjaguin–Muller–Toporov (DMT) model, for that reason called DMT modulus.

To probe liquid–surface interactions with maximum resolution, contact angles (at 22 °C) of small drops (four on each substrate) of diiodomethane (DIM, >99%, surface tension γ_l = 48.7 mN/m at 18.8 °C, ~1 μL), 1,2-ethanediol or ethylene glycol (EG, >99%, γ_l = 47.7 mN/m at 18.8 °C, ~1 μL), and filtered water (FW, γ_l = 73.4 mN/m at 18.8 °C, ~2 μL) placed on horizontal surfaces were measured by use of a contact angle goniometer (Kruss DSA30, Germany). Advancing angles (θ_A) were obtained for both “left” and “right” contact angles about 20–30 s after placement of the drop.²⁶ Surface energies (γ_s) of the probed solid surfaces were calculated from contact angles and interfacial energies (γ_l) of the three probe liquids by use of eqs 1–3²⁷ and an in-house Visual Basic program. Total surface energy is the sum of Lifshitz–van der Waals (also called dispersion or nonpolar) and acid–base (also called polar) contributions. The polar portion can be further subdivided into Lewis acid and Lewis base components.

$$\gamma_s = \gamma_s^{LW} + \gamma_s^{AB} = \gamma_s^{LW} + 2(\gamma_s^+ \gamma_s^-)^{0.5} \quad (1)$$

$$\gamma_l = \gamma_l^{LW} + \gamma_l^{AB} = \gamma_l^{LW} + 2(\gamma_l^+ \gamma_l^-)^{0.5} \quad (2)$$

$$\gamma_l(1 + \cos \theta) = 2[(\gamma_s^{LW} \gamma_l^{LW})^{0.5} + (\gamma_s^+ \gamma_l^-)^{0.5} + (\gamma_s^- \gamma_l^+)^{0.5}] \quad (3)$$

In eqs 1–3, superscripts denote components of the surface energy: LW, Lifshitz–van der Waals; AB, acid–base; γ⁺, Lewis acid; and γ⁻, Lewis base. In FW, γ_l^{LW} = 21.8 mJ/m² and γ_l⁺ = γ_l⁻ = 25.5 mJ/m²; in DIM, γ_l^{LW} = 50.8 mJ/m² and γ_l⁺ = γ_l⁻ = 0 mJ/m²; and in EG, γ_l^{LW} = 29 mJ/m², γ_l⁺ = 1.92 mJ/m², and γ_l⁻ = 47 mJ/m².²⁸

Six samples featuring both bottom-gate organic field-effect transistors (OFETs) and metal–insulator–metal (MIM) structures were fabricated side-by-side with the exception of thermal evaporation and desorption of alkylphosphonic acid (C_nPA). One C_nPA was used in each sample.

MIM and OFET structures followed the same fabrication procedure up to and including the phosphonic acid monolayer. All thermal evaporations (metals and organics) were performed in Mini-Spectros. First, 30 nm thick aluminum was evaporated on a glass substrate through a shadow mask. Part of each electrode was coated with 40 nm thick Au to prevent its oxidation. Next, all samples were exposed to UV/ozone to produce about 10 nm thick AlO_x. AlO_x was functionalized with C_nPA by the process described earlier. Some AlO_x was left uncoated to provide reference AlO_x MIM structures. Next, a 20 nm thick DNNTT layer was thermally evaporated at a rate of 0.5 Å/s at room temperature through a shadow mask. All MIM structures were masked during this step. Finally, a 50 nm thick Au layer was evaporated through a shadow mask at a rate of ~3 Å/s to

complete the transistors and MIM structures. The transistors have nominal channel lengths of 30, 50, 70, and 90 μm and a channel width of 1000 μm .

Transistor and MIM measurements were performed with an Agilent B1500A semiconductor device analyzer under dark ambient conditions. All fabricated devices were kept in oxygen- and moisture-free environment until their measurement, and they shared the same history. The gate dielectric capacitance of MIM structures was measured between 1 kHz and 1 MHz and extracted at 100 kHz. The MIM current density was measured as a function of applied voltage between -3 and 3 V. The transfer and output characteristics of the OFETs were measured in a sweep mode. The threshold voltage and field-effect mobility were extracted from the transfer characteristics measured in saturation by use of metal-oxide-semiconductor field-effect transistor (MOSFET) equations. Subthreshold slope, on-current, off-current, and on/off-current ratio were also extracted from the saturation curve. Mean values and standard deviations were calculated for all relevant transistor parameters. Bias stress was performed at $V_{\text{GS}} = -2$ V for 1000 s with source and drain electrodes grounded. At certain intervals, the bias stress was briefly interrupted and transistor transfer characteristics in saturation were measured to allow transistor parameter extraction.

Calculations were performed with density functional theory (DFT) as implemented in the Quantum Espresso (QE) package, version 5.1.²⁹ The core electrons were represented by use of projector-augmented wave potentials,³⁰ and valence electrons were represented with a plane-wave basis with cutoffs of 50 and 400 Ry for the wave functions and charge densities, respectively. The PBE version³¹ of the generalized gradient approximation was used for the exchange and correlation functional. Self-consistent calculations used an electronic convergence threshold of 1×10^{-8} Ry. Isolated molecules were generated with the aid of the chemical drawing tool Avogadro 1.1.1.³² The α -alumina (0001) slabs were six AlO_3Al layers thick, with a hexagonal lattice parameter of 4.80 Å. The top surface was terminated with an extra $\text{Al}(\text{OH})_3$ layer. Alkylphosphonic acid molecules with alkyl chain length from 2 to 18 carbon atoms were added on top of the relaxed Al_2O_3 (0001) hydroxylated surface with either monodentate or bidentate binding, by removing H atoms from the surface. The molecule, top AlO_3Al layer, and hydroxylated $\text{Al}(\text{OH})_3$ layer were allowed to relax until a force convergence threshold of 1×10^{-5} au was reached. A single k -point was used for the relaxation of isolated molecules, while a $3 \times 3 \times 1$ hexagonal k -point mesh was used when the surface was present. Periodic boundary conditions were implemented, and a vacuum layer of at least 7 Å was added on top of the molecules, to avoid self-interaction.

Vibration frequencies were calculated by use of the Phonon package in QE, and the self-consistency threshold was 1×10^{-14} Ry. For a few cases (free acids, C_{14}PA monodentate, and C_{18}PA mono- and bidentate), the self-consistency threshold was 1×10^{-18} Ry. The vibrational mode characters were assigned by visualizing individual vibrational modes with the Molden 5.3 package.³³ It is important to note that for some frequencies it was difficult to identify independent vibrational modes due to the interference of a wide range of vibrational modes occurring at similar frequencies. The vibration spectra were created by a superposition of Gaussians. Each Gaussian is centered at an identified vibration frequency and has a standard deviation of 10 cm^{-1} , and the area under the curve is proportional to the intensity of the mode.

3. RESULTS AND DISCUSSION

3.1. Gate Dielectric: Electrical and Structural Measurements. Figure 1a shows the capacitance of $\text{AlO}_x/\text{C}_n\text{PA}$ bilayers and the thickness calculated for each alkylphosphonic acid. Total dielectric capacitance (C_{diel}) consists of capacitance of the AlO_x layer (C_{AlO_x}) and capacitance of the phosphonic acid ($C_{\text{C}_n\text{PA}}$). The two capacitances are in series, therefore $1/C_{\text{diel}} = 1/C_{\text{AlO}_x} + 1/C_{\text{C}_n\text{PA}}$. This relationship can be rearranged to find

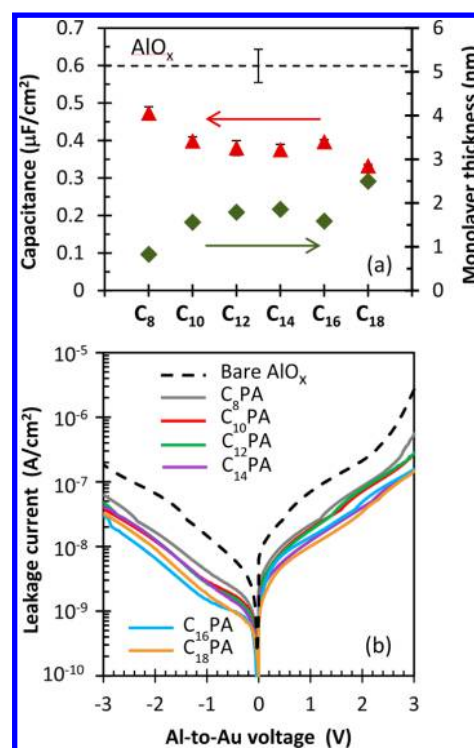


Figure 1. (a) $\text{AlO}_x/\text{C}_n\text{PA}$ capacitance and extracted C_nPA thickness versus C_nPA . AlO_x capacitance is given as a reference. (b) Current density of $\text{AlO}_x/\text{C}_n\text{PA}$ bilayers as a function of C_nPA . Bare AlO_x is included for comparison.

$C_{\text{C}_n\text{PA}}$, which is then used to calculate C_nPA thickness by using a relative permittivity value of 2.1.²¹ The capacitance of bare AlO_x has a mean value of $0.60 \mu\text{F}/\text{cm}^2$. $\text{AlO}_x/\text{C}_n\text{PA}$ capacitance is lower, and a decrease in capacitance per unit area is seen as C_nPA length increases. The increase in C_nPA thickness from 0.83 nm for C_8PA to 2.49 nm for C_{18}PA is consistent with the increased linear length of C_nPA molecules when n increases from 8 to 18.

AlO_x and $\text{AlO}_x/\text{C}_n\text{PA}$ leakage current densities for various phosphonic acids are shown in Figure 1b. Bare AlO_x dielectric displays a leakage current density of $\sim 2 \times 10^{-7}$ A/cm^2 at -3 V. At the same voltage, AlO_x functionalized with phosphonic acid shows reduced leakage current density with values between $\sim 6 \times 10^{-8}$ and $\sim 3 \times 10^{-8}$ A/cm^2 . Leakage current decreases as C_nPA length increases. In summary, both capacitance and leakage current measurements confirmed that the thickness of C_nPA increased with increasing n , while capacitance measurement determined that in all cases the C_nPA thickness corresponds to about a monolayer.

Water contact angles of $\text{AlO}_x/\text{C}_n\text{PA}$ as a function of C_nPA length are shown in Table 1a. After annealing to remove physisorbed molecules, all $\text{AlO}_x/\text{C}_n\text{PA}$ surfaces are hydrophobic, with water contact angles greater than 110° regardless of the alkyl chain length. Although a maximum value of $112.0^\circ \pm 1.1^\circ$ and a minimum value of $110.8^\circ \pm 1.3^\circ$ were obtained for C_{12}PA and C_{14}PA respectively, all contact angles are the same within the error of measurement. These contact angles were compared to a C_{18}PA layer prior to annealing, whose thickness of ~ 20 nm was confirmed by atomic force microscopy (AFM). This layer exhibits significantly different contact angles for all three liquids.

Table 1. (a) Advancing Contact Angles of Probe Liquids on Various Surfaces and (b) Surface Energies Calculated from These Contact Angles

(a) Contact Angles ^a				
surface	mean contact angle θ (deg)			
	FW	EG	DIM	
C ₈ PA	111.1 ± 0.2	70.4 ± 2.3	85.2 ± 0.8	
C ₁₀ PA	111.5 ± 0.9	71.4 ± 1.3	86.3 ± 2.6	
C ₁₂ PA	112.0 ± 1.1	70.9 ± 5.2	87.1 ± 1.9	
C ₁₄ PA	110.8 ± 1.3	71.2 ± 4.9	83.6 ± 1.6	
C ₁₆ PA	111.3 ± 0.8	68.7 ± 1.7	84.9 ± 1.1	
C ₁₈ PA	111.3 ± 0.8	70.8 ± 3.2	86.2 ± 1.0	
C ₁₈ PA ^c	77.4 ± 3.3	82.5 ± 0.4	70.7 ± 1.0	
(b) Surface Energies ^b (mJ/m ²)				
surface	γ_s^+	γ_s^-	γ_s^{LW}	γ_s
C ₈ PA	3.22	0.56	14.91	17.61 ± 1.1
C ₁₀ PA	3.18	0.53	14.39	16.98 ± 1.2
C ₁₂ PA	3.51	0.68	14.02	17.11 ± 2.2
C ₁₄ PA	2.73	0.44	15.69	17.89 ± 2.1
C ₁₆ PA	3.64	0.82	15.06	18.51 ± 1.1
C ₁₈ PA	3.30	0.55	14.44	17.13 ± 1.2
C ₁₈ PA ^c	0.67	27.23	22.48	31.03 ± 1.3

^aFW, filtered water; EG, ethylene glycol; DIM, diiodomethane. ^b γ_s^{LW} , Lifshitz–van der Waals; γ_s^+ , Lewis acid; γ_s^- , Lewis base. ^cPrior to annealing (~20 nm thick).

After annealing to remove physisorbed molecules, all AlO_x/C_nPA surfaces have low surface energy of ~17.5 mJ/m² with dominating Lifshitz–van der Waals (dispersive) component. No correlation between surface properties and length of the aliphatic chain is observed. The small Lewis acid component and negligible Lewis base component indicate that the surface has some electron-pair-accepting ability. On the contrary, surface energy of the ~20 nm thick C₁₈PA layer prior to annealing is much higher at ~31 mJ/m². The larger surface energy suggests that some C_nPA head groups are found on the surface. In this case the Lewis base component dominates (the surface has electron-pair-donating ability), followed by the sizable Lifshitz–van der Waals energy, which is about 50% higher than that of C_nPA monolayers after annealing. While C_nPA molecules are likely to be “standing up” in the monolayers as a result of their bonding to AlO_x, C₁₈PA molecules that form the top surface of a 20 nm thick layer are expected to assume random orientations, resulting in exposed –OH groups and different surface properties.

Comparing these results to those obtained for solution-assembled C_nPA, one would notice that solution-assembled

monolayers exhibit slightly lower contact angles for FW and DIM and higher surface energies ranging between 25 and 30 mJ/m².³⁴ However, this difference may result from the fact that ref 34 reports results for alkylphosphonic acids on sol-gel-derived hafnium oxide, while our results are for C_nPA on aluminum oxide.

AlO_x/C_nPA surfaces were also investigated by AFM (see Table 2). In addition to determining the root-mean-square (RMS) surface roughness, the use of a new PeakForce QNM scanning mode enabled direct extraction of quantitative nanomechanical information such as force of adhesion (F_{ad}), elastic modulus (E), deformation, and dissipation. The surface roughness (R_a) of ~10 nm thick AlO_x is 1.27 nm. The 3-h anneal at 160 °C does not affect its surface roughness, confirming that C_nPA desorption/annealing step would not lead to increased surface roughness of the AlO_x/C_nPA dielectric due to increased roughness of AlO_x. The surface roughness of AlO_x functionalized with C_nPA is comparable or slightly higher but below 2 nm in most cases. The C₁₈PA layer prior to annealing has a roughness of 2.25 nm. There is no correlation between AlO_x/C_nPA surface roughness and length of the phosphonic acid. In addition, no correlation is observed between C_nPA length and nanomechanical properties. Force values lie between ~3 and ~5 nN, moduli are between 22 and 63 GPa, deformation falls between ~3 and ~8 nm, and dissipation is between ~200 and 1000 eV. Previously, the surface roughness of alkylphosphonic acids, solution-assembled on top of Si/AlO_x, was affected by the length of the molecule, and the lowest surface roughness was achieved for C₁₄PA.¹⁴

In summary, AlO_x/C_nPA surfaces after annealing exhibit comparable RMS surface roughness. While their mechanical properties on the nanometer scale (AFM tip size is 2 nm) vary by a factor of 2–5 (see Table 2), their macroscopic surface properties (see Table 1) are similar.

Fourier transform infrared (FTIR) spectroscopy provides structural information on a macroscopic scale, that is, the scale of the transistor channel. FTIR was performed on AlO_x/C_nPA surfaces after annealing and on the reference AlO_x surface (see Figure 2). A strong broad absorbance near 900 cm⁻¹ is dominated by Al–O vibrations in all samples. Weaker vibrations are observed in the region from 1000 to 1250 cm⁻¹, near 1450 cm⁻¹, and between 2800 and 3000 cm⁻¹. In general, the integral intensity of various peaks is higher for shorter-chain C_nPA and lower for longer chains. As the length of the phosphonic acid is increased, the position of C–H₂ stretching is shifted to lower wavenumbers and their full width at half maximum (fwhm) is reduced. For C₈PA the peaks are centered at 2853 cm⁻¹ (fwhm = 20.7 cm⁻¹) and 2924 cm⁻¹

Table 2. Surface Roughness and Nanomechanical Properties Determined by AFM

surface	surface roughness (nm)	force (nN)	modulus (GPa)	deformation (nm)	dissipation (eV)
C ₈ PA	1.25	3.1 ± 0.7	63 ± 9	2.8 ± 0.6	353
C ₁₀ PA	1.53	3.6 ± 1.1	30 ± 9	3.2 ± 0.5	226
C ₁₂ PA	2.34	5.3 ± 1.6	28 ± 10	3.6 ± 0.7	1016
C ₁₄ PA	1.13	5.4 ± 1.5	29 ± 8	8.6 ± 2.5	277
C ₁₆ PA	1.82	2.8 ± 0.6	22 ± 5	4.0 ± 0.6	219
C ₁₈ PA	1.47	3.9 ± 1.0	37 ± 11	3.1 ± 0.1	945
C ₁₈ PA ^a	2.25	3.3 ± 1.2	65 ± 31	4.2 ± 1.1	566
AlO _x	1.27	4.9 ± 1.3	43 ± 10	4.4 ± 0.1	961
AlO _x ^b	1.22	4.9 ± 1.1	65 ± 50	4.5 ± 0.1	509

^aPrior to annealing (~20 nm thick). ^bAnnealed.

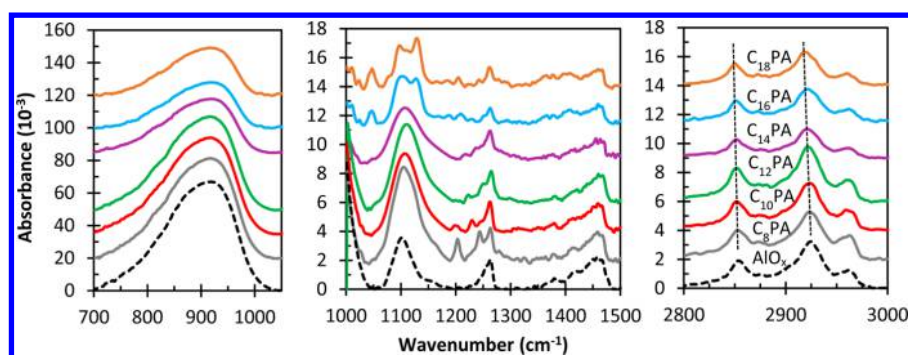


Figure 2. FTIR spectra of $\text{AlO}_x/\text{C}_n\text{PA}$ bilayers. Bare annealed AlO_x is included for comparison. Individual spectra are offset by a constant value to allow easier viewing.

($\text{fwhm} = 31.9 \text{ cm}^{-1}$), while for C_{18}PA the peaks are found at 2850 cm^{-1} ($\text{fwhm} = 17.3 \text{ cm}^{-1}$) and 2920 cm^{-1} ($\text{fwhm} = 28.4 \text{ cm}^{-1}$). These peak positions are very similar to those reported for C_nPA monolayers prepared in ethanol on hafnium oxide.³⁴ The shift in the peak location was previously interpreted as an improved molecular order within monolayers; that is, the increase in C_nPA length leads to stronger van der Waals interaction between aliphatic chains and results in a more ordered self-assembly with denser molecular packing.^{35–37} However, one would predict that the density of vacuum-deposited monolayers would be lower than that of solution-deposited monolayers as a result of the laws that govern physical vapor deposition. This is supported by the fact that the integral intensity of CH_2 stretches near 2850 and 2920 cm^{-1} does not increase with increasing length of C_nPA . As seen in Figure 2, the integral intensity of these spectral lines is comparable for C_8 , C_{10} , and C_{12}PA and lower for C_{14} , C_{16} , and C_{18}PA monolayers, suggesting lower molecular coverage for longer C_nPAs .

In summary, CH_2 stretching vibrations confirm that a degree of order exists even for vacuum-deposited monolayers, and the molecular order improves with increasing length of C_nPA . The spread in nanomechanical properties suggests heterogeneous monolayer structure, such as presence of domains or nanopores. Previously, molecular dynamic simulations performed on solution-assembled C_nPA monolayers on aluminum oxide confirmed a change in the morphology from amorphous to quasi-crystalline with increasing length of C_nPA .¹⁹ In such a case, highly ordered domains with gaps between them exist for long C_nPA molecules.

3.2. Organic Field-Effect Transistors: As Fabricated and Under Bias Stress. The cross-section of the bottom gate $\text{Al}/\text{AlO}_x/\text{C}_n\text{PA}/\text{DNTT}/\text{Au}$ transistor is shown in Figure 3a. Figure 3b shows transistor transfer characteristics for as-fabricated transistors with various phosphonic acid monolayers. As C_nPA length increases, threshold voltage (V_T) and transistor off-current (I_{off}) decrease. Figure 3c depicts output characteristics of an OFET with C_{18}PA and nominal channel length of $30 \mu\text{m}$. The behavior of all transistor parameters for as-fabricated transistors is shown in Figure 3d–i. Upon going from C_8PA to C_{18}PA , mean threshold voltage (V_T) decreases from -1.37 to -1.24 V , field-effect mobility (μ) increases from 0.03 to $0.33 \text{ cm}^2/(\text{V}\cdot\text{s})$, subthreshold slope (S) remains the same within the error of measurement (variation between 86 and $94 \text{ mV}/\text{decade}$), off-current (I_{off}) decreases from $\sim 8 \times 10^{-13}$ to $\sim 3 \times 10^{-13} \text{ A}$, and for OFETs with $L = 30 \mu\text{m}$, on-current (I_{on}) increases from $\sim 3 \times 10^{-8}$ to $\sim 2 \times 10^{-6} \text{ A}$ and on/off-current ratio ($I_{\text{on}}/I_{\text{off}}$) increases from $\sim 3 \times 10^4$ to $\sim 4 \times 10^6$.

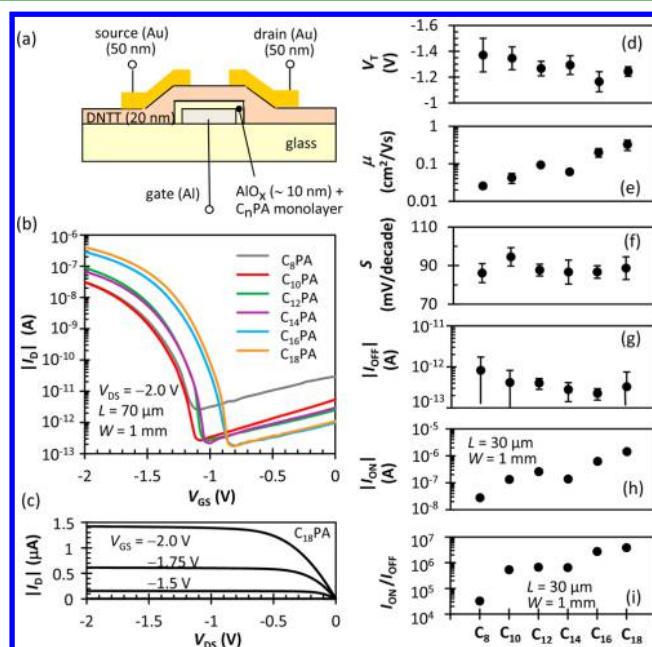


Figure 3. (a) OFET cross-section. (b) Transistor transfer characteristics as a function of C_nPA . (c) Transistor output characteristics for C_{18}PA . (d–i) Parameters of as-fabricated transistors as functions of C_nPA .

Overall, increasing length of the phosphonic acid leads to a significant improvement of transistor parameters. This behavior is different from the behavior of transistors that incorporated solution-assembled C_nPAs . For $\text{Si}/\text{HfO}_2/\text{C}_n\text{PA}/\text{pentacene}/\text{Au}$ OFETs, threshold voltage became more negative with increasing C_nPA length, while mobility of C_8 – C_{14}PA exceeded that of C_{16} – C_{18}PA .³⁴ For $\text{Si}/\text{AlO}_x/\text{C}_n\text{PA}/\text{pentacene}/\text{Au}$ OFETs, threshold voltage did not change significantly and mobility peaked for C_{14}PA .¹⁴ For $\text{Si}/\text{SiO}_2/\text{C}_n\text{PA}/\text{pentacene}/\text{Au}$ OFETs, the lowest threshold voltage occurred for C_8PA , mobility decreased from C_8PA to C_{18}PA , and subthreshold slope was unaffected.³⁸ For $\text{Al}/\text{AlO}_x/\text{C}_n\text{PA}/\text{pentacene}/\text{Au}$ OFETs, mobility peaked for C_{14}PA for oxygen-plasma AlO_x and increased with increasing C_nPA length for mild-air-plasma AlO_x .¹³ For $\text{Si}/\text{AlO}_x/\text{C}_n\text{PA}/\text{pentacene}/\text{Au}$ OFETs, both mobility and threshold voltage increased with increasing C_nPA length.¹⁹

Comparison of our C_{18}PA transistors to recently reported DNTT transistors that use other gate dielectrics is as follows. Cross-linked poly(ethylene-*alt*-maleic anhydride) (PEMA) led to a mobility of $0.11 \text{ cm}^2/(\text{V}\cdot\text{s})$, while PEMA modified with

poly(maleic anhydride-*alt*-1-octadecane) resulted in mobility of $0.24 \text{ cm}^2/(\text{V}\cdot\text{s})$.³⁹ Octylamine-treated PEMA gate dielectric led to mobility of $0.17 \text{ cm}^2/(\text{V}\cdot\text{s})$.⁴⁰ Vapor-jet-deposited DNTT on polystyrene-buffered poly(tripropylene glycol diacrylate) dielectric achieved a mobility of $0.43 \text{ cm}^2/(\text{V}\cdot\text{s})$.⁴¹ Field-effect mobilities in excess of $1 \text{ cm}^2/(\text{V}\cdot\text{s})$ were achieved when gate dielectrics incorporating organic monolayers were used.^{42–44} Threshold voltage and subthreshold slope depend on the thickness of the gate dielectric, and our values are consistent with the values achieved for other thin dielectrics. Similarly, comparison of the on/off ratio is difficult because it depends on transistor dimensions.

A short bias stress lasting for 1000 s was also performed. During the bias stress, a voltage of -2 V was applied to the gate while source and drain electrodes were grounded. All samples were kept in dark ambient air for 3 days before the bias stress was performed. Figure 4a shows the evolution of threshold

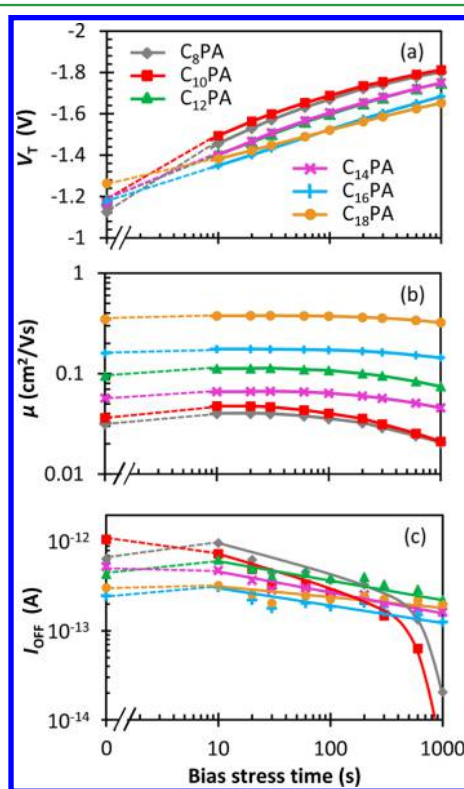


Figure 4. (a) Threshold voltage, (b) field-effect mobility, and (c) off-current as functions of bias stress time for transistors with various C_n PA.

voltage with increasing bias stress time. While transistors incorporating C_{16} PA and C_{18} PA monolayers exhibit initial threshold voltage similar to that shown in Figure 3, transistors with shorter phosphonic acids exhibit lower initial $|V_{T1}|$, indicating poorer ambient stability. Initial values of mobility and off-current are similar to those shown in Figure 3.

Bias stress leads to a more negative threshold voltage for all transistors; however, the rate of degradation decreases as length of the phosphonic acid increases, making transistors with C_{18} PA almost a factor of 2 more stable than those with C_8 PA. Degradation in field-effect mobility (see Figure 4b) exhibits different behavior for various C_n PA. For C_{18} PA and C_{16} PA, mobility exhibits only a minor change, reaching $\sim 93\%$ of the initial value at 1000 s. For C_{14} PA and C_{12} PA, mobility first

increases by about 20% and then decreases to about 80% of the initial value. For the shortest C_n PA, mobility first increases by 30–35% and then decreases to about 60% of the initial value. Off-current decreases for all C_n PA (see Figure 4c). While the decrease is almost negligible for longer C_n PA, the drop in I_{off} is much more pronounced for C_8 PA and C_{10} PA.

It has been shown that bias-stress degradation of DNTT transistors with polystyrene-buffered poly(tripropylene glycol diacrylate) dielectric depends on environmental conditions.²⁵ Since all our transistors were bias-stressed in the same laboratory environment (air, $\sim 40\%$ relative humidity), differences in their degradation are ascribed to transistor structure.

The choice of C_n PA affects gate dielectric capacitance (see Figure 1) and threshold voltage of the transistors (see Figure 3). Therefore, one should consider the induced capacitive charge at the beginning of the transistor bias-stress degradation. Since the gate-to-channel voltage is not known, the gate-to-source voltage V_{GS} is used to approximate the accumulated charge; that is, $Q = C |V_{\text{GS}} - V_{\text{T}}|$. This charge is $0.41 \mu\text{C}/\text{cm}^2$ for C_8 PA, $0.24 \mu\text{C}/\text{cm}^2$ for C_{18} PA, and $0.31\text{--}0.33 \mu\text{C}/\text{cm}^2$ for the remaining C_n PA. If transistor bias degradation were solely controlled by induced charge density, then transistors with C_{10} , C_{12} , C_{14} , and C_{16} PA should exhibit similar degradation behavior. However, the results of Figure 4 show degradation that is clearly linked to length of the phosphonic acid instead of induced charge density.

The experimental results confirm strong correlation between initial and bias-induced transistor behavior and length of the C_n PA monolayer. Overall, the transistors exhibit improved initial parameters and ambient and bias-stress stability when C_n PA length increases. FTIR vibrations between 2800 and 3000 cm^{-1} indicate a degree of order within the monolayer that improves with increasing C_n PA length. Our discussion will now focus on DFT results and parts of the FTIR spectra that “probe” the bonding of C_n PA to AlO_x .

3.3. Density Functional Theory. As shown above, water contact angles and surface energy are the same for all AlO_x/C_n PA surfaces after annealing. Minor differences in RMS surface roughness are not correlated to the length of C_n PA. However, FTIR spectra show differences and so does the transistor behavior. DFT was therefore used to calculate vibration frequencies of different C_n PA molecules in their free state as well as bonded to stoichiometric Al_2O_3 . Here, monodentate and bidentate bonding was considered.

Figure 5 shows sections of the vibration spectra calculated from DFT. Vibrations exist below 700 cm^{-1} ; however, this section is not shown as there are no experimental data to match it. For free acids, P–OH vibrations are located between ~ 800 and $\sim 850 \text{ cm}^{-1}$, P=O is found near 1250 cm^{-1} , and CH_3/CH_2 stretches occur between ~ 2930 and $\sim 3050 \text{ cm}^{-1}$. These frequencies can be compared with calculations from self-consistent charge density-functional tight binding (SCC-DFTB),⁴⁵ which is based on DFT but is a more approximate method. Such calculations gave P–OH vibrations in the range $625\text{--}683 \text{ cm}^{-1}$, P=O vibration of 1324 cm^{-1} , and CH_2/CH_3 vibrations in the region between 2750 and 3000 cm^{-1} . For monodentate attachment of C_n PA (see Figure 5), the region between 700 and 1000 cm^{-1} contains AlO, P–OAl, P–OH, and P–C vibrations. AlO–H bending and P=O stretching are both found near 1025 and 1150 cm^{-1} ; however, AlO–H bending contributes more strongly to the vibration at 1025 cm^{-1} , while P=O stretch dominates the vibration near 1150 cm^{-1} . C_n PA length does not affect the position of these peaks.

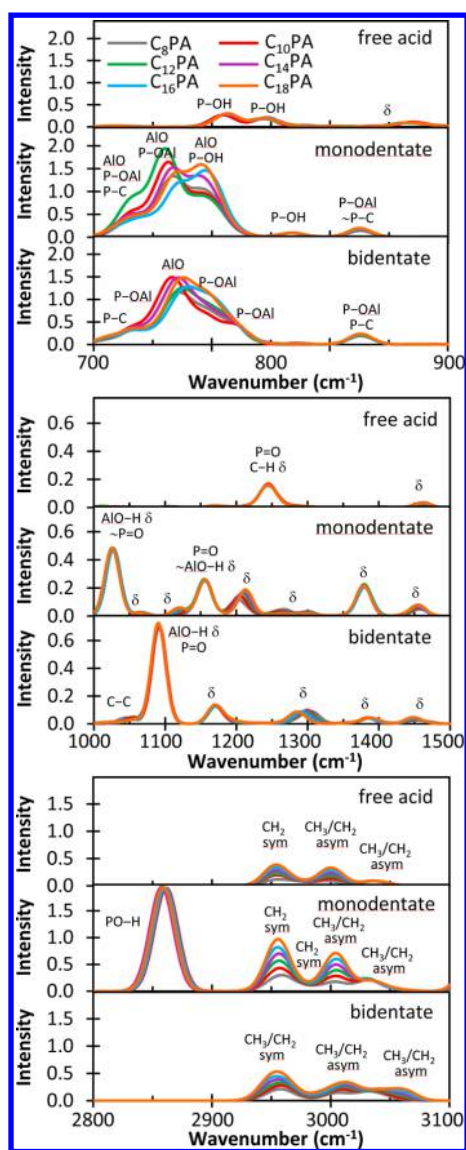


Figure 5. DFT vibration spectra for various C_n PAs, as free acids and for monodentate and bidentate attachments to stoichiometric Al_2O_3 . δ signifies a bending mode.

The two main CH_3/CH_2 stretches are pushed further apart due to CH_3/CH_2 asymmetric stretching being shifted to slightly higher wavenumbers. The $P=O$ frequency of 1150 cm^{-1} can be compared to the SCC-DFTB value of 1320 cm^{-1} for phosphonic acid $HPO(OH)_2$ on alumina⁴⁵ and to an experimental value of 1278 cm^{-1} for C_{18} PA acid on silicon.⁴⁶ DFT calculations of alkylphosphonic acids on silicon gave CH_3/CH_2 frequencies in the range $2925\text{--}3075\text{ cm}^{-1}$.⁴⁶ Finally, for bidentate attachment of C_n PA (see Figure 5), the region between 700 and 1000 cm^{-1} contains AIO, P-OAl, and P-C vibrations. AIO-H bending and $P=O$ stretch are both found near 1100 cm^{-1} , and C_n PA length does not affect the position or intensity of this peak. The two main CH_3/CH_2 stretches are pushed even further apart due to an additional shift of CH_3/CH_2 asymmetric stretching to higher wavenumbers. The second CH_3/CH_2 asymmetric stretch is also shifted to higher wavenumbers. For $HPO(OH)_2$ on alumina, SCC-DFTB gave the $P=O$ frequency as 1325 cm^{-1} , which is very similar to their monodentate value.⁴⁵

Compared to the measured data of Figure 2, calculated positions of CH_3/CH_2 stretches are shifted to higher wavenumbers for all bonded phosphonic acids. This could be for two reasons: (a) DFT approximation of exchange and correlation effects and (b) neglect of dynamic (finite temperature) effects. Inclusion of van der Waals interactions that partially account for electron correlation effects may improve the DFT results, as has been shown for the case of water.⁴⁷

Overall, the most significant differences in vibration spectra between monodentate and bidentate attachments are in the regions $750\text{--}800\text{ cm}^{-1}$ and $1000\text{--}1200\text{ cm}^{-1}$. While the former is buried in the strong AIO peak of measured FTIR spectra, the second region can be used to analyze the experimental data. DFT also showed that the tilt of C_n PA with respect to the surface normal decreases with increasing length of the molecule, and for any C_n PA the bidentate attachment results in a smaller tilt when compared to the monodentate attachment (see Supporting Information). Tilt angles are smaller than those predicted by the SCC-DFTB method,⁴⁸ but this is to be expected as our coverage is higher, forcing the molecules to be more upright.

Previous research has shown that phosphonic acids self-assembled from solutions strongly attach to aluminum oxide.⁴⁹ Attachment is facilitated by the headgroup that reacts with surface hydroxyl groups of aluminum oxide.⁵⁰ When the metal oxide surface possesses Lewis acidic sites, binding originates from coordination of $P=O$ to such a site, followed by the condensation reaction between P-OH and Al-OH moieties to produce P-O-Al bonds.⁵¹ This ultimately leads to tridentate C_n PA attachment. On metal oxides lacking Lewis acidity, reaction between P-OH and Al-OH moieties results in bidentate attachment.⁵¹ Tridentate attachment is also possible when a hydrogen bond between surface -OH and $P=O$ moieties is formed. Another proposed mechanism involves protonation of surface -OH groups followed by formation of the P-O-Al bond.^{48,52} In such a case, the phosphorus atom is left with a positive charge. In addition, DFT calculations have shown that the thermodynamically preferred binding mode depends on surface structure of the aluminum oxide and the amount of residual water.⁵³

DFT calculations show that monodentate binding of C_n PA to Al_2O_3 results in a strong PO-H vibration found below the region of CH_2/CH_3 stretches. Since measured FTIR spectra of all C_n PA monolayers lack such vibrations, monodentate attachment is unlikely for vacuum-deposited monolayers. This is further supported by the presence of a broad vibration band near 1100 cm^{-1} , consistent with bidentate bonding. DFT assigns this vibration band to AIO-H bending and $P=O$ stretching. The measured integral intensity of this band decreases with increasing C_n PA length, and the contributing vibration frequencies move slightly apart. This is interpreted as reduced C_n PA coverage because similar reduction in the integral intensity of CH_2 stretches is observed for longer C_n PA. This also agrees with the expected random orientation of C_n PA molecules during physical vapor deposition and the area each molecule is likely to occupy. Another possibility is that some $P=O$ bonds disappear as a result of tridentate attachment. However, if tridentate attachment occurred for longer C_n PA via protonation of surface -OH groups, the resulting immobile positive charge should lead to a more negative threshold voltage, which is not observed. Formation of a hydrogen bond between surface -OH and $P=O$ moieties is more plausible, because it would lead to a shift in AIO-H and $P=O$ vibration

frequencies and no immobile charge. Consequently, tridentate attachment via hydrogen bond cannot be excluded.

3.4. Final Remarks. We would like to make a few remarks about the observed transistor behavior. Negatively charged immobile species in the presence of hydroxyl groups were demonstrated in the case of Si–OH when silicon dioxide was used as gate dielectric⁵⁴ or as a result of electrochemical reactions that involve adsorbed water.⁵⁵ The presence of Al–OH groups on the surface of AlO_x could also lead to fixed negative charge located at the AlO_x/C_nPA interface. Since more Al–OH sites would be expected for longer C_nPA when fewer molecules are attached to AlO_x, lower threshold voltage is expected for longer C_nPA. This is indeed observed for as-fabricated transistors. However, the presence of Al–OH sites does not explain the different ambient and bias-stress degradations.

Phosphonic acids possess a dipole moment that has been shown to control the threshold voltage of the transistors.⁵⁶ The component normal to the AlO_x surface is quite small if the molecule stands perpendicular to the surface.⁵⁶ This component would change with length and tilt of the C_nPA molecule. Bending of the longer molecules observed by DFT would complicate matters even more. The existence of dipole moments can potentially explain the observed differences in $|V_T|$ for as-fabricated transistors. However, it cannot explain the different ambient and bias-stress degradations.

Another possibility involves the reduced density of C_nPA monolayers for longer molecules. Lower molecular coverage can be intentionally induced by substrate heating during C_nPA growth.²² Our previous experiments with C₈PA and pentacene showed an increase in $|V_T|$ and a decrease in field-effect mobility with increasing C₈PA growth temperature.²² This behavior is opposite to that observed in Figure 3, and therefore, varied molecular density is an unlikely cause of the change in threshold voltage.

Finally, changing morphology of the monolayers with increasing C_nPA length could have a profound effect on the growth of DNNT. The large increase in field-effect mobility and the dissimilar degradation behavior must be controlled by the C_nPA/DNNT interface and/or DNNT itself. Additional research is needed to understand how these vacuum-evaporated alkylphosphonic acids control the growth of DNNT.

4. CONCLUSION

Growth that self-limits the thickness of materials is desirable for ultrathin dielectrics for low-voltage transistors. In this paper, we showed that monolayers of alkylphosphonic acids (C₈–C₁₈) can be prepared by vacuum evaporation and incorporated into organic field-effect transistors based on DNNT.

AlO_x/C_nPA bilayers (~11–12 nm thick) exhibit low leakage current densities ranging between $\sim 6 \times 10^{-8}$ and $\sim 3 \times 10^{-8}$ A/cm² at –3 V. The decrease in capacitance with increasing length of C_nPA confirms monolayer formation for all phosphonic acids. Total surface energy of AlO_x/C_nPA surfaces after annealing is ~ 17.5 mJ/m² and independent of C_nPA length. All AlO_x/C_nPA surfaces exhibit comparable RMS surface roughness. While their macroscopic surface properties are similar, the mechanical properties on the nanometer scale vary by a factor of 2–5. Similarly to solution-assembled monolayers, the CH₂ stretching peaks narrow and shift to lower wavenumbers, confirming that molecular order improves with increasing length of C_nPA. At the same time, reduced molecular coverage appears for longer C_nPAs. The spread in nano-

mechanical properties suggests a heterogeneous monolayer structure, such as the presence of domains or nanopores.

Performance of as-fabricated transistors is affected considerably by the chosen C_nPA. Upon going from C₈PA to C₁₈PA, threshold voltage moves closer to zero by ~10%, field-effect mobility increases by an order of magnitude, off-current decreases by ~50%, and subthreshold slope does not visibly change. As a result, on-current and on/off-current ratio increase by 2 orders of magnitude for OFETs with $L = 30$ μm. Increasing C_nPA length leads to a significant improvement of transistor parameters. Results of bias stress also confirm that degradation behavior is linked to length of the phosphonic acid instead of induced charge density. As C_nPA length increases, transistors are less prone to bias stress. In addition, transistors with longer C_nPA exhibit better air stability.

DFT calculations show that bonding of C_nPA molecules (monodentate versus bidentate) results in different vibration frequencies between 1000 and 1200 cm⁻¹. Strong PO–H vibration is also present for monodentate bonding. Comparison of DFT results and FTIR measurements leads to the conclusion that monodentate bonding does not occur for any C_nPA.

■ ASSOCIATED CONTENT

Supporting Information

The Supporting Information is available free of charge on the ACS Publications website at DOI: 10.1021/acsami.6b08426.

Four figures showing images of relaxed phosphonic acids (C₁₀, C₁₄, and C₁₈) on alumina in monodentate and bidentate coordinations and comparison of DFT vibration spectra of phosphonic acids (C₂–C₁₈) free and bonded to alumina (PDF)

■ AUTHOR INFORMATION

Corresponding Authors

*(H.G.) E-mail helena.gleskova@strath.ac.uk.

*(K.J.) E-mail karen.johnston@strath.ac.uk.

Notes

The authors declare no competing financial interest.

■ ACKNOWLEDGMENTS

S.H. is a recipient of a doctoral training grant funded by the Engineering and Physical Sciences Research Council (EPSRC), Grant EP/L505080/1. J.C. was funded by a WISE Bridging the Gap project, University of Strathclyde. DFT results were obtained by use of the EPSRC-funded ARCHIE-WeSt High Performance Computer (www.archie-west.ac.uk); EPSRC Grant EP/K000586/1. FTIR analysis was developed within CENTEM project CZ.1.05/2.1.00/03.0088, cofunded by the ERDF and follow-up sustainability stage CENTEM+ (LO1402) under the National Sustainability Programme I.

■ REFERENCES

- (1) Fiore, V.; Battiato, P.; Abdinia, S.; Jacobs, S.; Chartier, I.; Coppard, R.; Klink, G.; Cantatore, E.; Ragonese, E.; Palmisano, G. An Integrated 13.56-MHz RFID Tag in a Printed Organic Complementary TFT Technology on Flexible Substrate. *IEEE Trans. Circuits Syst. I* **2015**, *62*, 1668–1677.
- (2) Cantatore, E.; Geuns, T. C. T.; Gelinck, G. H.; van Veenendaal, E.; Gruijthuisen, A. F. A.; Schrijnemakers, L.; Drews, D.; de Leeuw, D. M. A 13.56-MHz RFID System Based on Organic Transponders. *IEEE J. Solid-State Circuits* **2007**, *42*, 84–92.
- (3) Maiellaro, G.; Ragonese, E.; Castorina, A.; Jacob, S.; Benwadih, M.; Coppard, R.; Cantatore, E.; Palmisano, G. High-Gain Operational

Transconductance Amplifiers in a Printed Complementary Organic TFT Technology on Flexible Foil. *IEEE Trans. Circuits Syst. I* **2013**, *60*, 3117–3125.

(4) Marien, H.; Steyaert, M. S. J.; van Veenendaal, E.; Heremans, P. Analog Building Blocks for Organic Smart Sensor Systems in Organic Thin-Film Transistor Technology on Flexible Plastic Foil. *IEEE J. Solid-State Circuits* **2012**, *47*, 1712–1720.

(5) Crone, B.; Dodabalapur, A.; Lin, Y. Y.; Filas, R. W.; Bao, Z.; LaDuca, A.; Sarpeshkar, R.; Katz, H. E.; Li, W. Large-Scale Complementary Integrated Circuits Based on Organic Transistors. *Nature* **2000**, *403*, 521–523.

(6) Gelinck, G. H.; Huitema, H. E. A.; Van Veenendaal, E.; Cantatore, E.; Schrijnemakers, L.; Van der Putten, J. B. P. H.; Geuns, T. C. T.; Beenhakkers, M.; Giesbers, J. B.; Huisman, B. H.; Meijer, E. J.; Benito, E. M.; Touwslager, F. J.; Marsman, A. W.; Van Rens, B. J. E.; De Leeuw, D. M. Flexible Active-Matrix Displays and Shift Registers Based on Solution-Processed Organic Transistors. *Nat. Mater.* **2004**, *3*, 106–110.

(7) Maiellaro, G.; Ragonese, E.; Gwoziecki, R.; Jacobs, S.; Marjanovic, N.; Chrapa, M.; Schleuniger, J.; Palmisano, G. Ambient Light Organic Sensor in a Printed Complementary Organic TFT Technology on Flexible Plastic Foil. *IEEE Trans. Circuits Syst. I* **2014**, *61*, 1036–1043.

(8) Scarpa, G.; Idzko, A.-L.; Yadav, A.; Martin, E.; Thalhammer, S. Toward Cheap Disposable Sensing Devices for Biological Assays. *IEEE Trans. Nanotechnol.* **2010**, *9*, 527–532.

(9) Noguchi, Y.; Sekitani, Y.; Someya, T. Organic-Transistor-Based Flexible Pressure Sensors Using Ink-Jet-Printed Electrodes and Gate Dielectric Layers. *Appl. Phys. Lett.* **2006**, *89*, 253507.

(10) Halik, M. Gate Dielectrics. In *Organics Electronics: Materials, Manufacturing, and Applications*; Klauk, H., Ed.; Wiley-VCH: Weinheim, Germany, 2006; pp 132–162; DOI: [10.1002/3527608753.ch6](https://doi.org/10.1002/3527608753.ch6).

(11) Maliakal, G. Dielectric Materials: Selection and Design. In *Organic Field-Effect Transistors*; Bao, Z., Locklin, J., Eds.; CRC Press: Boca Raton, FL, 2007; pp 229–251.

(12) Klauk, H.; Zschieschang, U.; Pflaum, J.; Halik, M. Ultralow-Power Organic Complementary Circuits. *Nature* **2007**, *445*, 745–748.

(13) Jedaa, A.; Burkhardt, M.; Zschieschang, U.; Klauk, H.; Habich, D.; Schmid, G.; Halik, M. The Impact of Self-Assembled Monolayer Thickness in Hybrid Gate Dielectrics for Organic Thin-Film Transistors. *Org. Electron.* **2009**, *10*, 1442–1447.

(14) Fukuda, K.; Hamamoto, T.; Yokota, T.; Sekitani, T.; Zschieschang, U.; Klauk, H.; Someya, T. Effects of the Alkyl Chain Length in Phosphonic Acid Self-Assembled Monolayer Gate Dielectrics on the Performance and Stability of Low-Voltage Organic Thin-Film Transistors. *Appl. Phys. Lett.* **2009**, *95*, 203301.

(15) Acton, O.; Osaka, I.; Ting, G.; Hutchins, D.; Ma, H.; McCullough, R. D.; Jen, A. K.-Y. Phosphonic Acid Self-Assembled Monolayer and Amorphous Hafnium Oxide Hybrid Dielectric for High Performance Polymer Thin Film Transistors on Plastic Substrates. *Appl. Phys. Lett.* **2009**, *95*, 113305.

(16) Zschieschang, U.; Ante, F.; Yamamoto, T.; Takimiya, K.; Kuwabara, H.; Ikeda, M.; Sekitani, T.; Someya, T.; Kern, K.; Klauk, H. Flexible Low-Voltage Organic Transistors and Circuits Based on a High-Mobility Organic Semiconductor with Good Air Stability. *Adv. Mater.* **2010**, *22*, 982–985.

(17) Wöbkenberg, P. H.; Ball, J.; Kooistra, F. B.; Hummelen, J. C.; de Leeuw, D. M.; Bradley, D. D. C.; Anthopoulos, T. D. Low-Voltage Organic Transistors Based on Solution Processed Semiconductors and Self-Assembled Monolayer Gate Dielectrics. *Appl. Phys. Lett.* **2008**, *93*, 013303.

(18) Fukuda, K.; Yokota, T.; Kuribara, K.; Sekitani, T.; Zschieschang, U.; Klauk, H.; Someya, T. Thermal Stability of Organic Thin-Film Transistors with Self-Assembled Monolayer Dielectrics. *Appl. Phys. Lett.* **2010**, *96*, 053302.

(19) Novak, M.; Jäger, C. M.; Rumpel, A.; Kropp, H.; Peukert, W.; Clark, T.; Halik, M. The Morphology of Integrated Self-Assembled

Monolayers and Their Impact on Devices - A Computational and Experimental Approach. *Org. Electron.* **2010**, *11*, 1476–1482.

(20) Urasinska-Wojcik, B.; Cocherel, N.; Wilson, R.; Burroughes, J.; Opoku, J.; Turner, M. L.; Majewski, L. A. 1 V Organic Transistors with Mixed Self-Assembled Monolayer/ Al_2O_3 Gate Dielectrics. *Org. Electron.* **2015**, *26*, 20–24.

(21) Gupta, S.; Gleskova, H. Dry Growth of n-Octylphosphonic Acid Monolayer for Low-Voltage Organic Thin-Film Transistors. *Org. Electron.* **2013**, *14*, 354–361.

(22) Gupta, S.; Šutta, P.; Lamprou, D. A.; Gleskova, H. Effect of Substrate Temperature on Vapor-Phase Self-Assembly of n-Octylphosphonic Acid Monolayer for Low-Voltage Organic Thin-Film Transistors. *Org. Electron.* **2013**, *14*, 2468–2475.

(23) Gleskova, H.; Gupta, S.; Šutta, P. Structural Changes in Vapor-Assembled n-Octylphosphonic Acid Monolayer with Post-Deposition Annealing: Correlation with Bias-Induced Transistor Instability. *Org. Electron.* **2013**, *14*, 3000–3006.

(24) Milvich, J.; Zaki, T.; Aghamohammadi, M.; Rödel, R.; Kraft, U.; Klauk, H.; Burghartz, J. N. Flexible Low-Voltage Organic Phototransistors Based on Air-Stable Dinaphtho[2,3-b:2',3'-f]thieno[3,2-b]thiophene (DNFTT). *Org. Electron.* **2015**, *20*, 63–68.

(25) Ding, Z.; Abbas, G.; Assender, H. E.; Morrison, J. J.; Yeates, S. G.; Patchett, E. R.; Taylor, D. M. Effect of Oxygen, Moisture and Illumination on the Stability and Reliability of Dinaphtho[2,3-b:2',3'-f]thieno[3,2-b]thiophene (DNFTT) OTFTs during Operation and Storage. *ACS Appl. Mater. Interfaces* **2014**, *6*, 15224–15231.

(26) Adamson, W.; Gast, A. P. *Physical Chemistry of Surfaces*; Wiley-Interscience: New York, 1997.

(27) Zisman, W. A. Relation of the Equilibrium Contact Angle to Liquid and Solid Constitution. In *Contact Angle, Wettability, and Adhesion*; Gould, R. F., Ed.; Advances in Chemistry, Volume 43; American Chemical Society: Washington, DC, 1964; pp 1–51; DOI: [10.1021/ba-1964-0043.ch001](https://doi.org/10.1021/ba-1964-0043.ch001).

(28) Janczuk, B.; Bialopiotrowicz, T.; Zdziennicka, A. Some Remarks on the Components of the Liquid Surface Free Energy. *J. Colloid Interface Sci.* **1999**, *211*, 96–103.

(29) Giannozzi, P.; Baroni, S.; Bonini, N.; Calandra, M.; Car, R.; Cavazzoni, C.; Ceresoli, D.; Chiarotti, G. L.; Cococcioni, M.; Dabo, I.; Dal Corso, A.; de Gironcoli, S.; Fabris, S.; Fratesi, G.; Gebauer, R.; Gerstmann, U.; Gougoussis, C.; Kokalj, A.; Lazzeri, M.; Martin-Samos, L.; Marzari, N.; Mauri, F.; Mazzarello, R.; Paolini, S.; Pasquarello, A.; Paulatto, L.; Sbraccia, C.; Scandolo, S.; Sclauzero, G.; Seitonen, A. P.; Smogunov, A.; Umari, P.; Wentzcovitch, R. M. J. QUANTUM ESPRESSO: A Modular and Open-Source Software Project for Quantum Simulations of Materials. *J. Phys.: Condens. Matter* **2009**, *21*, No. 395502.

(30) Blochl, P. E. Projector Augmented-Wave Method. *Phys. Rev. B: Condens. Matter Mater. Phys.* **1994**, *50*, 17953–17979.

(31) Perdew, J. P.; Burke, K.; Ernzerhof, M. Generalized Gradient Approximation Made Simple. *Phys. Rev. Lett.* **1996**, *77*, 3865–3868.

(32) Hanwell, M.; Curtis, D. E.; Lonie, D. C.; Vandermeersch, T.; Zurek, E.; Hutchison, G. R. Avogadro: An Advanced Semantic Chemical Editor, Visualization, and Analysis Platform. *J. Cheminf.* **2012**, *4*, 17.

(33) Schafteenaar, G.; Noordik, J. H. Molden: A Pre- and Post-Processing Program for Molecular and Electronic Structures. *J. Comput.-Aided Mol. Des.* **2000**, *14*, 123–134.

(34) Acton, O.; Ting, G. G.; Shamberger, P. J.; Ohuchi, F. S.; Ma, H.; Jen, A. K.-Y. Dielectric Surface-Controlled Low-Voltage Organic Transistors via n-Alkyl Phosphonic Acid Self-Assembled Monolayers on High-k Metal Oxide. *ACS Appl. Mater. Interfaces* **2010**, *2*, 511–520.

(35) Love, J. C.; Estroff, L. A.; Kriebel, J. K.; Nuzzo, R. G.; Whitesides, G. M. Self-Assembled Monolayers of Thiolates on Metals as a Form of Nanotechnology. *Chem. Rev.* **2005**, *105*, 1103–1169.

(36) Schreiber, F. Structure and Growth of Self-Assembling Monolayers. *Prog. Surf. Sci.* **2000**, *65*, 151–256.

(37) Nuzzo, R. G.; Dubois, L. H.; Allara, D. L. Fundamental Studies of Microscopic Wetting on Organic Surfaces 0.1. Formation and

Structural Characterization of a Self-Consistent Series of Polyfunctional Organic Monolayers. *J. Am. Chem. Soc.* **1990**, *112*, 558–569.

(38) Hill, I. G.; Weinert, C. M.; Kreplak, L.; van Zyl, B. P. Influence of Self-Assembled Monolayer Chain Length on Modified Gate Dielectric Pentacene Thin-Film Transistors. *Appl. Phys. A: Mater. Sci. Process.* **2009**, *95*, 81–87.

(39) Yoo, S.; Yi, M. H.; Kim, Y. H.; Jang, K.-S. One-Pot Surface Modification of Poly(ethylene-alt-maleic anhydride) Gate Insulators for Low-Voltage DNTT Thin-Film Transistors. *Org. Electron.* **2016**, *33*, 263–268.

(40) Choe, Y.-S.; Yi, M. H.; Kim, J.-H.; Kim, Y. H.; Jang, K.-S. Surface Grafting of Octylamine onto Poly(ethylene-alt-maleic anhydride) Gate Insulators for Low-Voltage DNTT Thin-Film Transistors. *Phys. Chem. Chem. Phys.* **2016**, *18*, 8522–8528.

(41) Ding, Z.; Abbas, G. A. W.; Assender, H. E.; Morrison, J. J.; Yeates, S. G.; Patchett, E. R.; Taylor, D. M. Vacuum Production of OTFTs by Vapor Jet Deposition of Dinaphtho [2,3-b:2',3'-f]thieno[3,2-b]thiophene (DNTT) on a Lauryl Acrylate Functionalized Dielectric Surface. *Org. Electron.* **2016**, *31*, 90–97.

(42) Zschieschang, U.; Ante, F.; Kälblein, D.; Yamamoto, T.; Takimiya, K.; Kuwabara, H.; Ikeda, M.; Sekitani, T.; Someya, T.; Blochwitz-Nimoth, J.; Klauk, H. Dinaphtho[2,3-b:2',3'-f]thieno[3,2-b]thiophene (DNTT) Thin-Film Transistors With Improved Performance and Stability. *Org. Electron.* **2011**, *12*, 1370–1375.

(43) Chang, H.; Deng, Y.; Geng, Y.; Wang, T.; Yan, D. Effect of the Initial Stage of Film Growth on Device Performance of Organic Transistors Based on Dinaphtho[2,3-b:2',3'-f]thieno[3,2-b]thiophene (DNTT). *Org. Electron.* **2015**, *22*, 86–91.

(44) Zhang, Z.; Ren, X.; Peng, B.; Wang, Z.; Wang, X.; Pei, K.; Shan, B.; Miao, Q.; Chan, P. K. L. Direct Patterning of Self-Assembled Monolayers by Stamp Printing Method and Applications in High Performance Organic Field-Effect Transistors and Complementary Inverters. *Adv. Funct. Mater.* **2015**, *25*, 6112–6121.

(45) Luschtinetz, R.; Seifert, G.; Jaehne, E.; Adler, H.-J. P. Infrared Spectra of Alkyl Phosphonic Acid Bound to Aluminum Surfaces. *Macromol. Symp.* **2007**, *254*, 248–253.

(46) Longo, R. C.; Cho, K.; Schmidt, W. G.; Chabal, Y. J.; Thissen, P. Monolayer Doping via Phosphonic Acid Grafting on Silicon: Microscopic Insight from Infrared Spectroscopy and Density Functional Theory Calculations. *Adv. Funct. Mater.* **2013**, *23*, 3471–3477.

(47) Zhang, C.; Wu, J.; Galli, G.; Gygi, F. Structural and Vibrational Properties of Liquid Water from van der Waals Density Functionals. *J. Chem. Theory Comput.* **2011**, *7*, 3054–3061.

(48) Luschtinetz, R.; Oliveira, A. F.; Duarte, H. A.; Seifert, G. Self-assembled Monolayers of Alkylphosphonic Acids on Aluminum Oxide Surfaces – A Theoretical Study. *Z. Anorg. Allg. Chem.* **2010**, *636*, 1506–1512.

(49) Hoque, E.; DeRose, J. A.; Kulik, G.; Hoffmann, P.; Mathieu, H. J.; Bhushan, B. Alkylphosphonate Modified Aluminum Oxide Surfaces. *J. Phys. Chem. B* **2006**, *110*, 10855–10861.

(50) Giza, M.; Thissen, P.; Grundmeier, G. Adsorption Kinetics of Organo-Phosphonic Acids on Plasma-Modified Oxide-Covered Aluminum Surfaces. *Langmuir* **2008**, *24*, 8688–8694.

(51) Pujari, S. P.; Scheres, L.; Marcelis, A. T. M.; Zuillhof, H. Covalent Surface Modifications of Oxide Surfaces. *Angew. Chem., Int. Ed.* **2014**, *53*, 6322–6356.

(52) Luschtinetz, R.; Oliveira, A. F.; Frenzel, J.; Joswig, J.-O.; Seifert, G.; Duarte, H. A. Adsorption of Phosphonic and Ethylphosphonic Acid on Aluminum Oxide Surfaces. *Surf. Sci.* **2008**, *602*, 1347–1359.

(53) Bauer, T.; Schmaltz, T.; Lenz, T.; Halik, M.; Meyer, B.; Clark, T. Phosphonate- and Carboxylate-Based Self-Assembled Monolayers for Organic Devices: A Theoretical Study of Surface Binding on Aluminum Oxide with Experimental Support. *ACS Appl. Mater. Interfaces* **2013**, *5*, 6073–6080.

(54) Chua, L.-L.; Zaumseil, J.; Chang, J.-F.; Ou, E. C.-W.; Ho, P. K.-H.; Sirringhaus, H.; Friend, R. H. General Observation of N-type Field-Effect Behavior in Organic Semiconductors. *Nature* **2005**, *434*, 194–199.

(55) Bobbert, P. A.; Sharma, A.; Mathijssen, S. G. J.; Kemerink, M.; de Leeuw, D. M. Operational Stability of Organic Field-Effect Transistors. *Adv. Mater.* **2012**, *24*, 1146–1158.

(56) Amin, A. Y.; Reuter, K.; Meyer-Friedrichsen, T.; Halik, M. Interface Engineering in High-Performance Low-Voltage Organic Thin-Film Transistors Based on 2,7-Dialkyl-[1]benzothieno[3,2-b][1]benzothiophenes. *Langmuir* **2011**, *27*, 15340–15344.